Materials Advances

ROYAL SOCIETY OF CHEMISTRY

PAPER

View Article Online
View Journal | View Issue

Cite this: *Mater. Adv.*, 2021, 2, 3971

Controllable synthesis of self-templated hierarchical Ni_3S_2@N-doped carbon for enhanced oxygen evolution reaction†

Shuai Wang,[a] Zheng Lu,[a] Yuan Fang,[a] Tian Zheng,[b] Zidong Zhang,[a] Wenjian Wang,[a] Rui Zhao *[a] and Weidong Xue *[a]

Received 16th March 2021,
Accepted 15th April 2021

DOI: 10.1039/d1ma00229e

rsc.li/materials-advances

Rational construction of self-supporting electrodes has been extensively investigated in energy conversion and storage. In this work, hierarchical N-doped carbon-encapsulated Ni_3S_2 grown on a 3D porous Ni foam (H-Ni_3S_2@NC/NF) was controllably synthesized by a one-pot self-templated solvothermal method. Herein, we highlight the self-templated growth of multilayered Ni_3S_2 with N-doped carbon intercalation at a certain temperature. The unique H-Ni_3S_2@NC/NF shows enhanced active sites and a modulated electronic structure, which facilitates mass/electron transport. Thereby, the H-Ni_3S_2@NC outperforms a lower overpotential of 238 mV at 10 mA cm^{-2} and a low Tafel slope of 62 mV dec^{-1} than that of binary and ternary metal sulfides, suggesting an excellent mono-metal sulfide as a self-supporting electrode for oxygen evolution reaction.

1 Introduction

The rapid development of human productivity greatly accelerates the unbalance of traditional fossil fuels and ecosystems. The demand for energy conversion technology accompanied by sustainable energy resources is extremely urgent.[1] Electrocatalytic water splitting has been considered as a potential energy technology for the high acceptance of diverse energy units such as solar, wind, nuclear and tidal-based energy systems, converting intermittent energy resources to storable H_2 energy, and applied to pollution-free energy devices.[2,3] However, the efficiency of H_2 production is largely restricted by its anodic oxygen evolution reaction (OER, $4OH^- \rightarrow O_2 + 2H_2O + 4e^-$), which has also been extensively investigated in numerous energy fields such as metal-air cells and fuel cells.[4] The key issue in the OER process is the sluggish kinetics of uphill energy barrier for the O═O bond formation, leading to excessive cost for large-scale production.[5] To date, IrO_2 and RuO_2 are proverbially acknowledged as benchmark electrocatalysts for water oxidation, while their high cost and rare reservation limit industrial water splitting.[6] Hence, it is urgent to develop efficient OER electrocatalysts with low cost and high abundance.

Recently, self-supporting Ni_3S_2 materials have aroused widespread attention in energy fields due to their intrinsic conductivity, electrocatalytic activity and fabricability.[7] Ni foams are the most widely used substrate for in-situ growth of Ni_3S_2 due to its porous 3D framework, binder-free nature and nickel supplementary.[8] As far as we know, metal atom introduction, anion doping and carbon compounds are effective strategies to improve the electrocatalytic activity of Ni_3S_2 due to the morphology modification electronic redistribution and synergistic effect of metal atoms. On the one hand, different metal modifications lead to tremendous diversity in morphology by a hydrothermal/solvothermal method, for instance, nanoneedle-like Fe-doped Ni_3S_2/NF,[9] nanosheet-like Co/Ce–Ni_3S_2/NF,[10] diamond-like Mo–Ni_3S_2/NF and particle-like Mo/Mn–Ni_xS_y/NF.[11] However, the construction of well-designed morphology is exactly decided by complicated synthesis parameters such as reaction temperature, time, sulfur source and heteroatom.[12,13] In addition, the catalytic active central of the resulting binary and ternary metal sulfides is difficult to be distinguished. On the other hand, the anion doping and carbon compounds, for instance, N-, F-doping, and introduction of CNTs or graphenes, mainly work on the regulation of electronic redistribution, adsorption/desorption energy, and enhanced conductivity due to larger electronegativity than that of transition metals.[14–16] Generally, the preparation of anion doping and carbon composites is carried out by a multi-step process or high-temperature calcination with additional nitrogen-containing precursors, leading to high cost and safety concerns.[17,18] Therefore, facile preparation and systematic

[a] School of Materials and Energy, University of Electronic Science and Technology of China, Chengdu 610054, China. E-mail: ruizhao@uestc.edu.cn, xuewd@uestc.edu.cn
[b] State Key Laboratory of Environment-Friendly Energy Materials, Southwest University of Science and Technology, Mianyang, 621010, China

† Electronic supplementary information (ESI) available. See DOI: 10.1039/d1ma00229e

exploration of Ni_3S_2 compounded with N-doped carbon are significant to the deep understanding of the growth mechanism and improved electrocatalytic activity.

In this work, hierarchical Ni_3S_2 with N-doped carbon intercalation grown on the NF was systematically prepared by a self-templated solvothermal method at a certain temperature and time. Specifically, Ni_3S_2 exhibits a nanosheet-like morphology at first, and with the increase in reaction temperature and time, it forms multilayer structured Ni_3S_2 compounded with N-doped carbon, resulting in high conductivity and enlarged active sites. The unique morphology and modified electronic structure are highly expected to witness a favorable electrocatalytic performance of H-Ni_3S_2@NC/NF for alkaline water splitting.

2 Experimental section

2.1 Chemical reagents

KOH, HCl, Na_2S, $NiCl_2$ $6H_2O$, $Ni(NO_3)_2$ $6H_2O$, $NiSO_4$ $6H_2O$, $Ni(CH_3COO)_2$ $4H_2O$, thiourea (TU), ethylene glycol (EG), ethanol and acetone were of analytical grade and purchased from Chengdu Kelong Chemical Reagent Factory (Chengdu, China). Ruthenium oxide (RuO_2) was purchased from Shanghai Macklin Biochemical Co., Ltd (Shanghai, China). Nafion solution (5 wt%) was purchased from Shanghai Aladdin Biochemical Technology Co., Ltd (Shanghai, China). NF was purchased from Jinan Henghua Chemical Reagent Factory (Jinan, China).

2.2 Synthesis of hierarchical H-Ni_3S_2@NC/NF

Briefly, 1.0 mmol of TU and 0.3 mmol of $NiCl_2$ $6H_2O$ were dispersed in 50 mL EG and then transferred into a 100 mL Teflon-lined stainless autoclave. Subsequently, a piece of pretreated NF substrate (1 cm × 2 cm) was vertically put into the above solution and maintained at 160 °C for 8 h. Finally, after cooling to room temperature, the modified NF was alternately rinsed several times with deionized water and ethanol, and then dried in a vacuum oven at 60 °C for 8 h, which was named H-Ni_3S_2@NC-3/NF. As comparison, $NiCl_2$ $6H_2O$ with different contents of 0, 0.1, and 0.5 mmol was employed to prepare Ni_3S_2/NF and H-Ni_3S_2@NC-*X*/NF (*X* = 1 and 5), respectively. The obtained samples were used as the working electrode, and the average areal mass loading of active materials was weighed as 3.1 mg cm^{-2}.

2.3 Synthesis of A-Ni_3S_2/C

The optimal H-Ni_3S_2@NC-3/NF was selected to explore the self-templated growth by the annealing process. One piece of H-Ni_3S_2@NC-3/NF was heated to 500, 600 and 700 °C at a rate of 10 °C min^{-1} in argon atmosphere and maintained at this temperature for 2 h, which was named A-Ni_3S_2/C-500, A-Ni_3S_2/C-600, and A-Ni_3S_2/C-700, respectively.

2.4 Synthesis of RuO_2/NF

First, 10 mg of RuO_2 was dispersed in 750 μL of ethanol and 250 μL of deionized water under ultrasonication for 20 min. Subsequently, 50 μL of Nafion solution (5 wt%) was added into the above suspension for continuous ultrasonication. After that, 326 μL of uniform mixture was loaded on the pretreated NF and dried in a vacuum oven at 60 °C for 8 h.

2.5 Material characterization

X-Ray diffraction (XRD) was conducted using an X'Pert PRO diffractometer with Cu Kα radiation (λ = 1.54056 Å). Field emission scanning electron microscopy (FESEM) was carried out using a Carl Zeiss AG instrument. Transmission electron microscopy (TEM), high-resolution transmission electron microscopy (HRTEM), selected area electron diffraction (SAED), high-angle annular dark field scanning transmission electron microscopy (HAADF-STEM) and the corresponding energy-dispersive spectroscopic (EDS) mapping analysis were performed using a FEITecnai G2 F30. X-Ray photoelectron spectroscopy (XPS) was conducted using a Thermo Scientific instrument with Al K_α radiation. Raman spectrum of H-Ni_3S_2@NC-3/NF was recorded using a Renishaw spectrometer with a 532 nm laser as an excitation source. Fourier transform infrared (FTIR) spectra of H-Ni_3S_2@NC-3/NF were recorded using a Nicolet 5700 in the wavenumber range of 4000–400 cm^{-1}.

2.6 Electrocatalytic performance measurement

All electrochemical tests were conducted using a classic three-electrode system (CHI 660D, Chenhua), with a graphite rod and a Hg/HgO electrode as the counter and reference electrodes, respectively. The as-prepared H-Ni_3S_2@NC/NF, A-Ni_3S_2/C and RuO_2/NF were used as the working electrode. The OER polarization curves were evaluated by linear sweep voltammetry (LSV) at a scan rate of 1 mV s^{-1} in 1.0 M KOH solution. A Tafel slope was derived from the linear part of polarization curve based on the Tafel equation: $\eta = b\log j + a$, where η is the overpotential, j is the current density, and b is the Tafel slope. Cyclic voltammetry (CV) was employed to evaluate double-layer capacitance (C_{dl}) in the potential region of 1.22–1.32 V at different scan rates of 5–120 mV s^{-1}. Electrochemical impedance spectroscopy (EIS) was measured from 10^5 to 10^{-1} Hz with an amplitude potential of 5 mV. Long-term stability was evaluated by the *i*–*t* test at a constant potential of 1.47 V for 20 h. All potentials were *iR* corrected and converted into the RHE potential by the following equation: $E_{RHE} = E_{Hg/HgO} + 0.059 \times pH + 0.098$ V, pH = 14.

3 Results and discussion

3.1 Morphology and chemical structure

As shown in Fig. 1a, hierarchical H-Ni_3S_2@NC-3/NF can be facilely obtained by a self-templated solvothermal method. The unique H-Ni_3S_2@NC-3/NF is composed of broccoli-like microspheres and multilayered polyhedrons with a size of 1–2 μm and 10–30 μm, respectively (Fig. 1b). As shown in Fig. 1c and d, the microspheres are assembled with nanosheets while polyhedrons are constructed layer by layer with nanosheets homogeneously presented on their surface. It is generally acknowledged

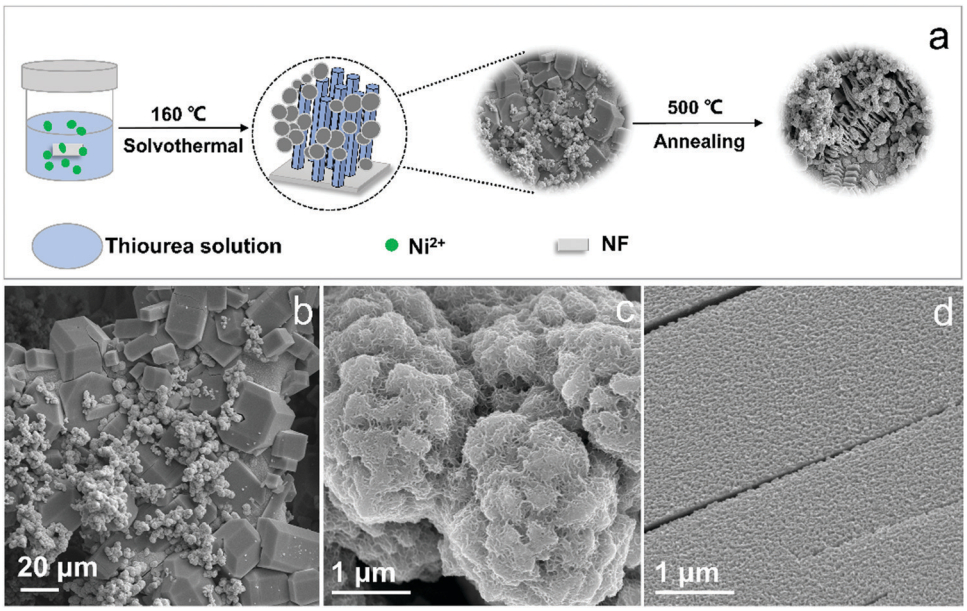

Fig. 1 Schematic of the preparation (a) and SEM images (b–d) of H-Ni_3S_2@NC-3/NF at different magnifications.

that nanomaterials possess special photoelectric/physical/chemical properties, which are beneficial for the electrocatalytic process.

Here, the H-Ni_3S_2@NC-3/NF material with a micro-nano structure benefits the OER process thanks to the following reasons: (i) the hierarchically assembled surface structure leads to more exposed active sites; (ii) the layered polyhedrons offer multi-pathways for fast charge transfer; and (iii) N-doped carbon gives rise to a modified electronic structure.[19] The EDS spectra of H-Ni_3S_2@NC-3/NF in Fig. S1 (ESI†) illustrate the presence of Ni and S elements on the microsphere and Ni, S, N, C, and O elements on the polyhedron, indicating the self-templated synthesis of a nickel–thiourea coordination complex that induces carbon intercalation.

Comparatively, Ni_3S_2/NF obtained without the addition of the Ni^{2+} precursor shows a nanocoral-like morphology (Fig. S2a and b, ESI†). The EDS spectrum and elemental mapping images shown in Fig. S2c–f (ESI†) display only Ni and S elements on its surface, revealing the significance of the Ni^{2+} precursor for the formation of N-doped carbon. The crystalline structures of Ni_3S_2/NF and H-Ni_3S_2@NC-3/NF are demonstrated in Fig. 2a. The peaks at 21.87°, 31.33°, 38.06°, 50.15° and 55.52° are indexed to the (101), (110), (003), (113) and (122) planes of hexagonal Ni_3S_2 (JCPDS No. 44-1418), respectively.[20,21] The peaks at 44.87°, 52.19° and 76.63° are ascribed to the (111), (200) and (220) planes of NF (JCPDS No. 04-0850).[22] The broad peak at 23.65° is assigned to carbon (JCPDS No. 46-0945).[23]

The phase structure was further characterized by Raman spectrum. As illustrated in Fig. S5a (ESI†), the bands at 220, 300, and 350 cm^{-1} represent the excitation bands of Ni_3S_2 whereas peaks located at around 1374 and 1598 cm^{-1} correspond to D and G bands of carbon, respectively.[24,25] The low I_D/I_G value of 0.56 indicates the introduction of graphitic carbon into Ni_3S_2 materials, which suggests smoother electron communication between multilayered polyhedron. Fig. S5b (ESI†) delivers the FTIR spectrum of H-Ni_3S_2/NF-0.3, where the absorption bands at 1052 and 1390 cm^{-1} are assigned to conjugated C–C and C–O stretching vibration.[26] The characteristic bands at 2172 and 1625 cm^{-1} indicate the presence of C≡N and C=N, whereas the bands at 3433 and 875 cm^{-1} are related to the stretching vibrations of C–OH and C–S, suggesting the successful intercalation of N-doped carbon.[27]

To have a deeper understanding of composition and phase structure of H-Ni_3S_2@NC-3/NF, active materials scraped from the NF substrate are obtained for TEM, HRTEM, SAED and EDS analysis. Fig. 2c and d show the TEM images for broccoli-like microspheres and multilayered polyhedrons, respectively. The broccoli-like microspheres exhibit an obvious nanosheet morphology with diffraction spots shown in the SAED pattern (inset of Fig. 2c), which corresponds to the (202), (122), (113) and (042) planes of Ni_3S_2, as evidenced by the XRD pattern above. In addition, the HRTEM image (Fig. 2e) indicates the characteristic lattice fringes of crystal Ni_3S_2 and parts of amorphous states. As for polyhedrons, amorphous states are observed in the SAED pattern (inset of Fig. 2d) and HRTEM image (Fig. 2f) due to the N-doped carbon intercalation, which is consistent with the EDS spectrum (Fig. 2b), HAADF-STEM image and elemental mapping analysis (Fig. S3, ESI†).

The composition and chemical valences of Ni_3S_2/NF and H-Ni_3S_2@NC-3/NF are characterized by XPS measurement. The survey spectrum of Ni_3S_2/NF (Fig. S4a, ESI†) suggests the presence of Ni, S, C and O. In the high-resolution Ni 2p spectrum (Fig. S4b, ESI†), the peaks at 855.74 and 873.38 eV are assigned to Ni $2p_{3/2}$ and Ni $2p_{1/2}$, whereas 861.06 and 879.41 eV are attributed to their shakeup satellites (identified as "Sat."). [28] The peaks at 852.43 and 869.65 eV are attributed to metal Ni that originated from the NF substrate.[29] In the high-resolution S 2p spectrum (Fig. S4c, ESI†), the peaks at 162.11 and 163.36 eV are assigned to S $2p_{3/2}$ and S–metal bond, respectively.[30]

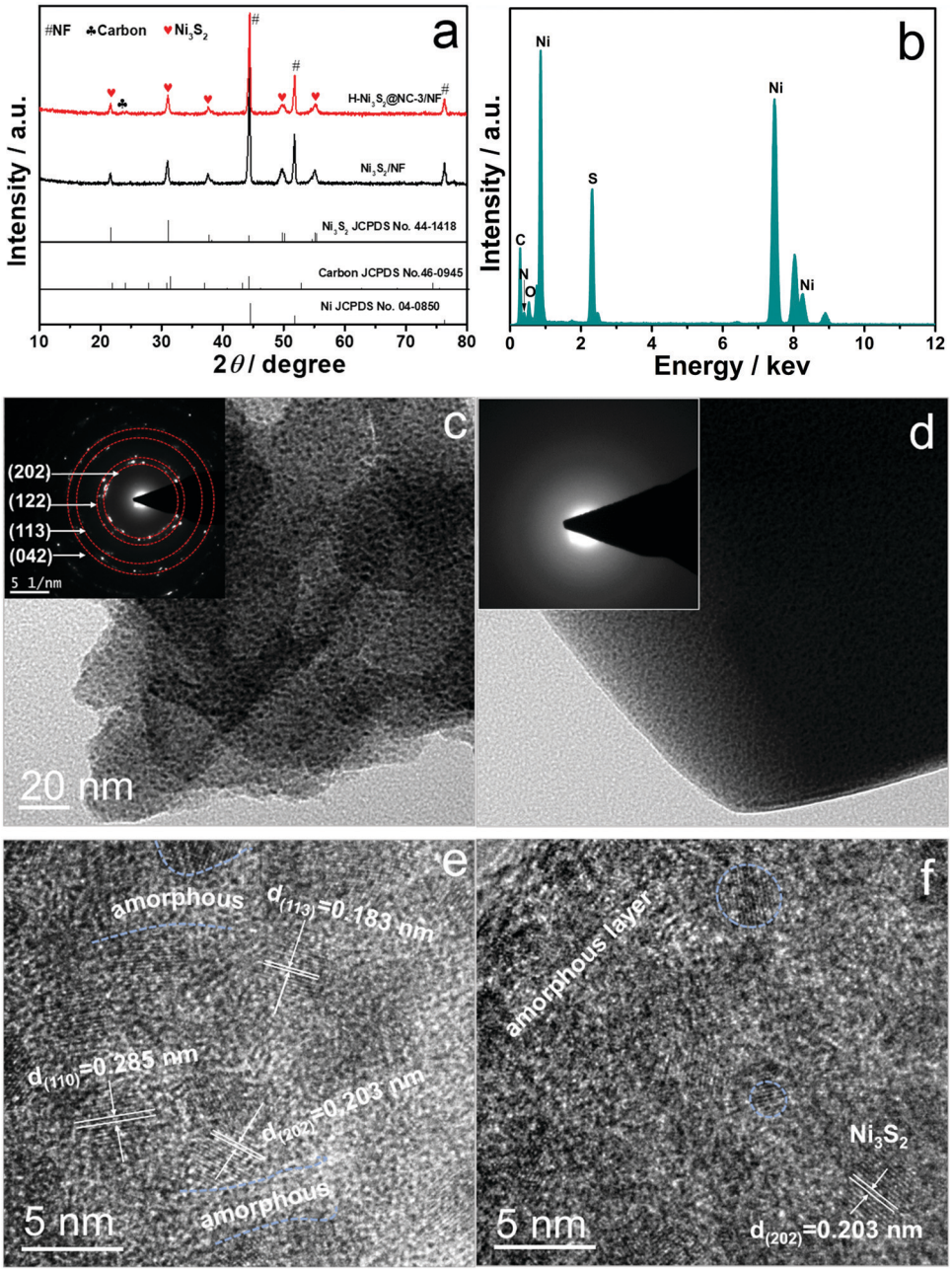

Fig. 2 XRD patterns (a) of Ni_3S_2/NF and H-Ni_3S_2@NC-3/NF; EDS spectrum (b) of H-Ni_3S_2@NC-3/NF; TEM with SAED patterns (inset of c and d), and HRTEM images for broccoli-like Ni_3S_2 (c and e) and multilayered polyhedrons (d and f), respectively.

As for H-Ni_3S_2@NC-3/NF, the XPS survey spectrum shown in Fig. 3a exhibits Ni, S, C, N and O elements. The presence of N elements suggests successful N-doping and, more importantly, the controllable structure formation induced by the nickel-TU coordination complex.[31] In high-resolution Ni 2p spectrum (Fig. 3b), the peaks at 855.84 and 873.54 eV are ascribed to Ni $2p_{3/2}$ and Ni $2p_{1/2}$, respectively.[32] The other peaks at 852.48 and 869.76 eV are indexed to metal Ni. The peaks located at 861.22 and 879.57 eV are assigned to Ni 2p (Sat.). The XPS spectrum of S 2p shown in Fig. 3c displays three peaks at 161.80, 162.95 and 165.60 eV, attributing to S $2p_{3/2}$, S–metal bond and surface oxidation.[33] The XPS spectrum of N 1s (Fig. 3d) displays a characteristic peak of C–N=C at 398.26 eV, suggesting the existence of N elements in H-Ni_3S_2@NC-3/NF.[34] The XPS spectrum of C 1s (Fig. 3e) reveals the presence of C=C/C–C (284.40 eV), C–N/C–S (285.43 eV) and O=C–O (288.31 eV).[35,36] Similarly, XPS spectrum of O 1s (Fig. 3f) shows the characteristic O=C at 532.03 eV, and the peak at 530.57 eV is assigned to metal–oxygen.[37] Here, TU served as N and C precursor bridges with nickel salts in the presence of porous NF, leading to reconstructed microspheres and multilayered polyhedrons on NF spontaneously. This unprecedented morphology and electronic structure are convenient for ion diffusion and charge transfer.[38]

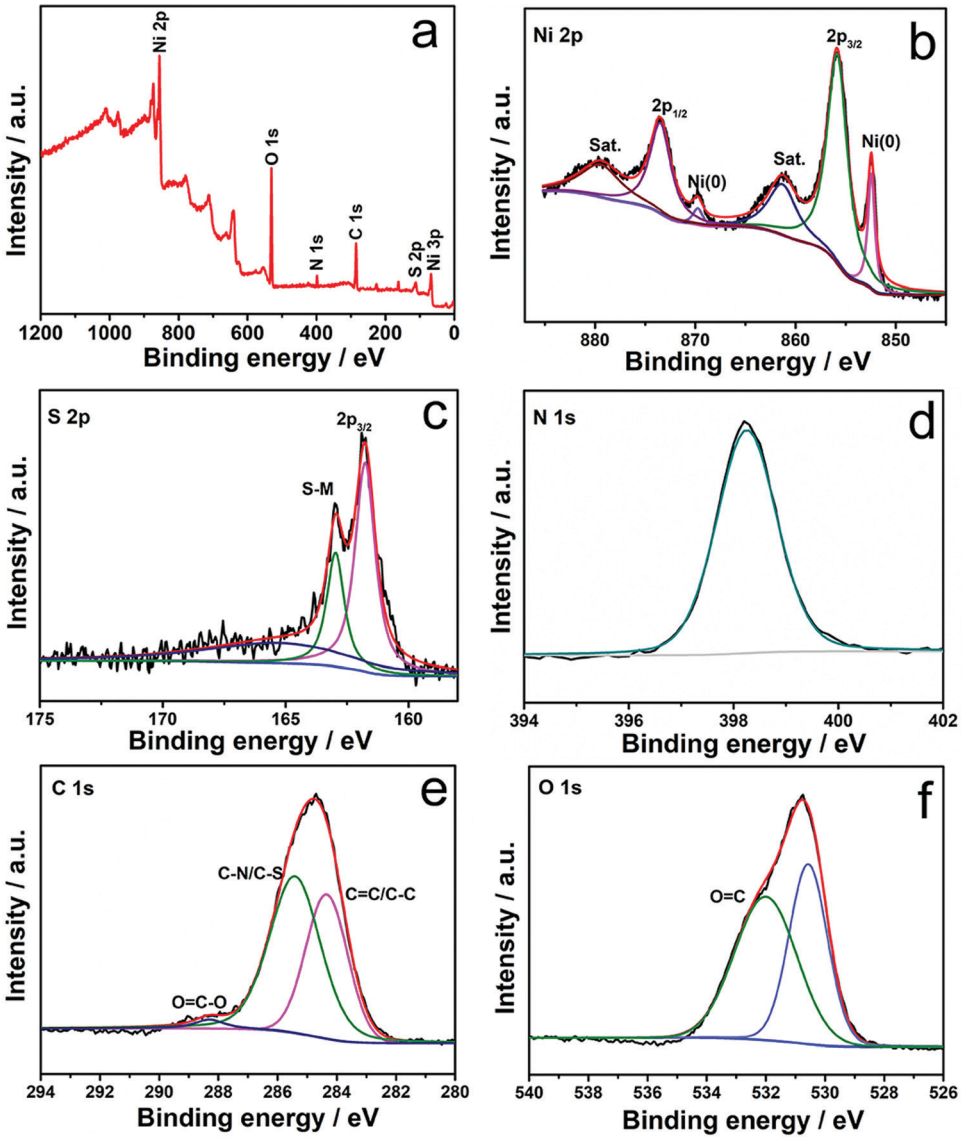

Fig. 3 XPS survey spectra (a) and high-resolution XPS spectra of Ni 2p (b), S 2p (c), N 1s (d), C 1s (e), and O 1s (f) for H-Ni_3S_2@NC-3/NF.

3.2 Growth mechanism

Surprisingly, the addition of Ni^{2+} precursor leads to extensive difference in composition and morphology. The unique formation of polyhedrons on NF by a self-templated solvothermal method has been rarely reported. We speculate that the addition of Ni^{2+} acts as a structure-directing agent, resulting in the coexistence of microspheres and polyhedrons. To further investigate the growth mechanism of H-Ni_3S_2@NC-3/NF, contrast experiments are systematically carried out based on the reaction temperature, time, metal substrate, as well as $Ni^{2+}$and S sources. Ultimately, the formation mechanism is proposed that the Ni^{2+} precursor coordinates with TU to form multilayered polyhedrons with simultaneous growth of nanosheet-reconstructed microspheres on the NF driven by different diffusion rates of nickel in reaction systems.

The formation of H-Ni_3S_2@NC-3/NF presents high reliance on temperature (Fig. 4). The SEM images in Fig. S6 (ESI†) verify the successful synthesis of H-Ni_3S_2@NC-3/NF at 150, 160, 170, and 180 °C although in a relatively irregular shape, while some polyhedrons on the NF prepared at 180 °C show the tendency of

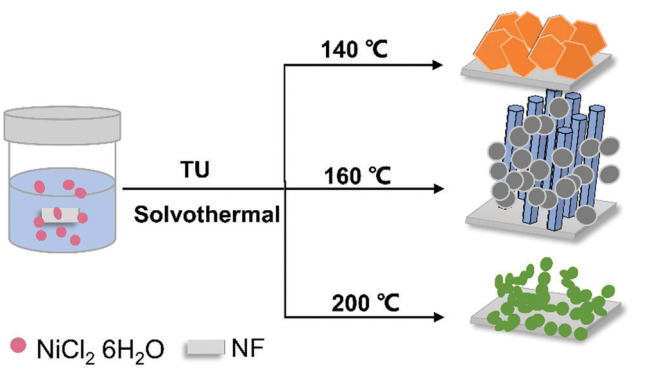

Fig. 4 Schematic of the preparation of H-Ni_3S_2@NC-3/NF at 140, 160 and 200 °C for 8 h.

structural collapse. In addition, only nanosheets and microspheres presented at 140 and 200 °C, respectively. This phenomenon indicates a temperature-dependent synthesis of H-Ni_3S_2@NC-3/NF, which means that thiourea releases H_2S etching NF to form nanosheet-like Ni_3S_2 at 140 °C. In the region of 150–180 °C, H_2S etching NF accompanied by the isomerization of thiourea and nickel ion coordination complexes leads to hierarchical N-doped carbon-encapsulated Ni_3S_2. When the temperature reaches 200 °C, only microsphere-like Ni_3S_2 presented on NF, which may be due to the melting of thiourea. The crystalline structure of samples obtained at 140, 160 and 200 °C is assigned to hexagonal Ni_3S_2 (JCPDS No. 44-1418), suggesting the facile construction of Ni_3S_2 at different temperatures (Fig. S7a, ESI†). It is noted that the optimal temperature is decided by OER performance, as shown in Fig. S7b (ESI†). H-Ni_3S_2@NC-3/NF prepared at 160 °C shows great electroactivity with a lower overpotential and a higher current density, which may be due to the synergistic effect of the internal highly active nanoparticles with the exposed (110) plane of Ni_3S_2 and the outer N-doped carbon in the sample, resulting in enhanced active sites on the catalyst surface.[39]

With the increase in reaction time, nanosheets accumulate to micron-sized polyhedrons. In detail, the Ni^{2+} precursor coordinated with TU leads to multilayer stacked nanosheets on NF in the first 2 h (Fig. S8a, ESI†) due to the abundant dangling bond on the surface of the 2D interlayer. Subsequently, smaller-sized nanosheets reconstruct to larger-sized polyhedrons with increasing layer thickness as time goes on (Fig. S8b–d, ESI†). Simultaneously, microsphere-like Ni_3S_2 grows on the NF by the diffusion rate difference based on adding Ni^{2+} and NF substrates. Here, TU as a complexing agent offers C, N and S elements, achieving an obvious polyhedral structure with N-doped carbon intercalation. In order to investigate the effect of the NF substrate and TU on hybrid formation, a Ni plate (NP), carbon cloth (CC) and Na_2S were used as alternatives in the process of H-Ni_3S_2@NC-3/NF, and named H-Ni_3S_2/NP, Ni_3S_2/CC and Ni_3S_2/NF nanoparticles, respectively. Evidently, the NF substrate is the key to anchor the position of polyhedrons. As shown in Fig. S9 (ESI†), H-Ni_3S_2/NP presents little amounts of polyhedrons on dense NP, revealing propense anchoring on porous substrates. However, Ni_3S_2/CC shows the absence of polyhedrons due to the inert substrate of CC, indicating the importance of the 3D porous Ni substrate. Ni_3S_2/NF nanoparticles prepared by Na_2S confirm the significant coordination of nickel–TU, resulting in innovative polyhedrons. By the light of Ni^{2+} precursors for the formation of polyhedrons, other nickel salts are studied to verify the consistent synthesis route. As displayed in Fig. S10 (ESI†), three kinds of nickel salts as Ni^{2+} precursors all successfully induced the formation of polyhedrons, except for differences in shape and surface in details. The above-mentioned results prove the nickel–TU-induced controllable synthesis of polyhedrons under certain reaction conditions.

The annealing process is carried out to manifest the bridge-interlayer structure of polyhedrons. The H-Ni_3S_2@NC-3/NF are heated at 500, 600 and 700 °C in argon atmosphere and named A-Ni_3S_2/C-500, A-Ni_3S_2/C-600, A-Ni_3S_2/C-700, respectively. The porous NF skeleton of A-Ni_3S_2/C-700 completely collapsed at high temperatures. Interestingly, polyhedrons exfoliate to accordion-like morphology with the decrescent volume, which is attributed to the broken C–N/C–S bridge bonds under the annealing process, resulting in a weak interface of layers (Fig. S11a–c, ESI†). Moreover, A-Ni_3S_2/C-500 and A-Ni_3S_2/C-600 consist of Ni, S and C elements with obvious loss of N elements, which further proves the significance of nickel-TU template–induced growth (Fig. S11d, ESI†). The lower electrocatalytic activity of A-Ni_3S_2/C-500 and A-Ni_3S_2/C-600 than that of H-Ni_3S_2@NC-3/NF may be due to the dilapidation of the hierarchical structure with N loss and amorphous states (Fig. S12, ESI†). Comparison of the above-mentioned studies confirms the accordance between growth mechanism and reaction parameters, where Ni^{2+} acts as a structure-directing agent, TU the self-templated bridging materials, and NF the anchor substrate within the temperature range of 150–180 °C. Hence, this new synthesis route is expected to manufacture well-designed nanostructures with great electrocatalytic performance for oxygen evolution reaction.

3.3 Electrocatalytic performance

As illustrated above, H-Ni_3S_2@NC/NF can be controllably fabricated by a solvothermal method under certain conditions. Therefore, H-Ni_3S_2@NC/NF with different amounts of Ni^{2+} precursors were prepared, and the corresponding SEM images are shown in Fig. S13 (ESI†). With the increase in the amount of Ni^{2+} precursors, more polyhedrons are observed grown on the NF and the corresponding OER properties are obtained by polarization curves at 1 mV s^{-1} in 1.0 M KOH solution. As shown in Fig. S14 (ESI†), the peak at approximately 1.4 V belongs to the oxidation of Ni.[40] Clearly, H-Ni_3S_2@NC-3/NF exhibits better OER performance with a lower overpotential and a higher current density. To achieve the current density of 10 mA cm^{-2}, H-Ni_3S_2@NC-3/NF shows a lower overpotential of 238 mV than H-Ni_3S_2@NC-1/NF (270 mV) and H-Ni_3S_2@NC-5/NF (260 mV), suggesting the synergetic effect of the microsphere and polyhedron structure on OER electroactivity. Herein, the optimal H-Ni_3S_2@NC-3/NF was adopted to have a deep OER mechanism over Ni_3S_2/NF, bare NF and RuO_2/NF by LSV, Tafel slope, CV, EIS and *i–t* measurements in the following process.

Polarization curves of H-Ni_3S_2@NC-3/NF, Ni_3S_2/NF, bare NF and RuO_2/NF are obtained at a scan rate of 1 mV s^{-1} in 1.0 M KOH solution (Fig. 5a). Ni_3S_2/NF displays enhanced OER performance with a lower potential and a higher current density than those of bare NF, suggesting the intrinsic activity of Ni_3S_2 materials. However, Ni_3S_2/NF exhibits an unsatisfactory potential of 1.75 V inferior to RuO_2/NF. When adding Ni^{2+}, the obtained H-Ni_3S_2@NC-3/NF shows better electroactivity of 1.59 V at a current density of 50 mA cm^{-2} than Ni_3S_2/NF and RuO_2/NF. Compared with Ni_3S_2/NF, a positive shift of Ni 2p and a negative shift of S 2p are observed in Fig. S15 (ESI†) for H-Ni_3S_2@NC-3/NF due to the strong electronegativity of N, indicating the successful N-doping-modified electronic structure.[16]

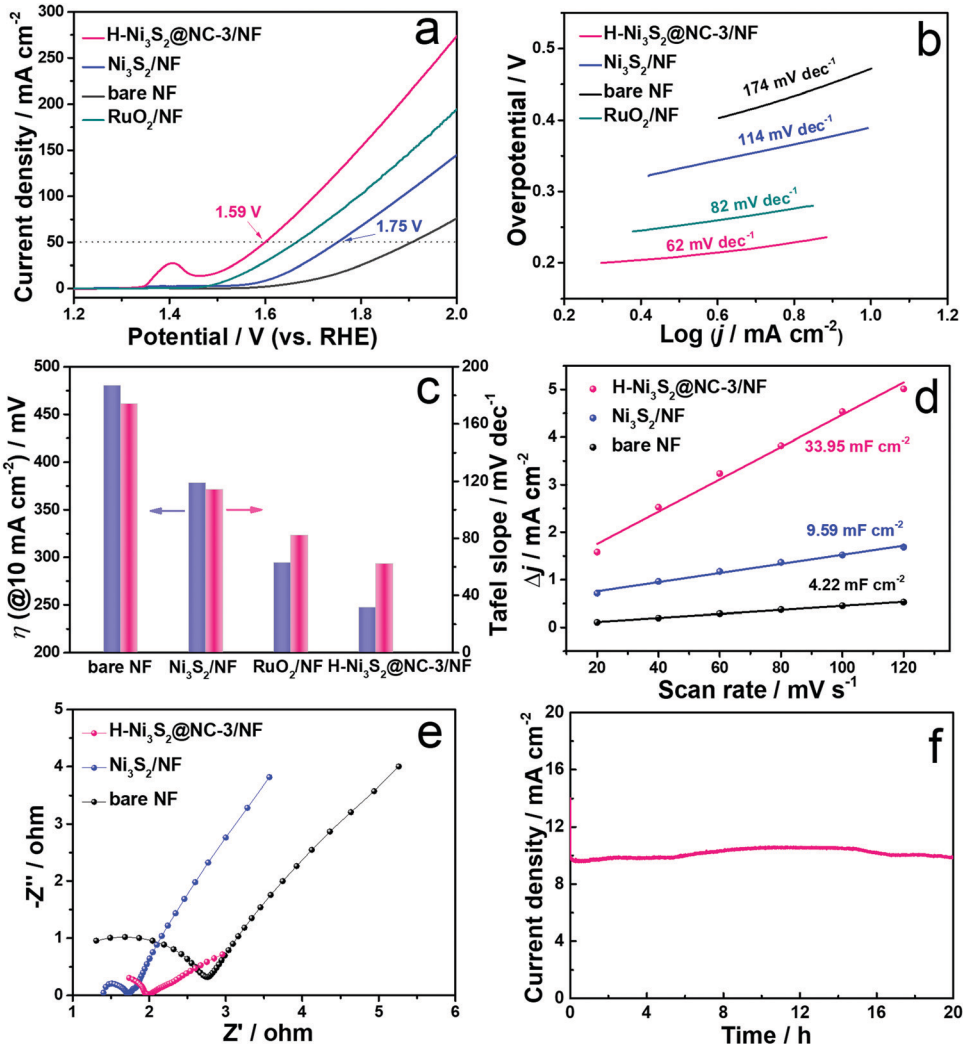

Fig. 5 Polarization curves (a), Tafel slope (b), comparison of η_{10} and Tafel value (c), C_{dl} plots (d), Nyquist plots (e) of H-Ni_3S_2@NC-3/NF, Ni_3S_2/NF and bare NF, long-term stability (f) of H-Ni_3S_2@NC-3/NF for 20 h.

The intensity of Ni(0) for H-Ni_3S_2@NC-3/NF is lower than Ni_3S_2/NF, suggesting the structure agent of Ni^{2+} leads to more high valence of Ni on the surface of H-Ni_3S_2@NC-3/NF. As well known, the high valence of transition metal promotes the charge transfer of intermediates on the catalyst surface. In addition, the superior performance of the catalyst is highly relevant to the morphology structure, crystal phase and electronic structure, thereby resulting in effective active sites and suitable adsorption/desorption energy.[41] The excellent OER performance of H-Ni_3S_2@NC-3/NF is attributed to the following reason: (i) nanosized surface engineering of microspheres and multilayer polyhedrons; (ii) amorphous states observed in HRTEM images and (iii) N atom–modified electronic structure.

To elucidate the kinetics of the as-prepared materials, Tafel slopes were acquired deriving from polarization curves. As presented in Fig. 5b, H-Ni_3S_2@NC-3/NF shows a Tafel slope of 62 mV dec^{-1}, while RuO_2/NF, Ni_3S_2/NF and bare NF display a Tafel slope of 82, 114 and 174 mV dec^{-1}, respectively. The lower value of Tafel slope indicates fast charge transfer between the intermediates and the catalyst surface. The comparison of overpotential at 10 mA cm^{-2} and the corresponding Tafel slope for the as-prepared materials are described in Fig. 5c, suggesting considerable electroactivity of H-Ni_3S_2@NC-3/NF among RuO_2/NF, Ni_3S_2/NF and bare NF.

To further explore the intrinsic OER electroactivity, CV curves are performed at a scan rate of 5–120 mV s^{-1} (Fig. S16, ESI†). Double-layer capacitances (C_{dl}) shown in Fig. 5d are plotted by the difference between the current density and the scan rate, which is positively correlated with the electrochemical surface area (ECSA). As expected, H-Ni_3S_2@NC-3/NF (33. 95 mF cm^{-2}) exhibits 3.5 times higher C_{dl} value than that of Ni_3S_2/NF (9.59 mF cm^{-2}) and bare NF (4.22 mF cm^{-2}). The high C_{dl} value indicates large ECSA and enriched active sites, which is consistent with the results of polarization curves. EIS was carried out at an AC-amplitude of 5 mV and the corresponding fitted Nyquist plots are displayed in Fig. 5e. The Nyquist plots consist of the high-frequency semicircle and the low-frequency straight line, where the semicircle stands for charge transfer

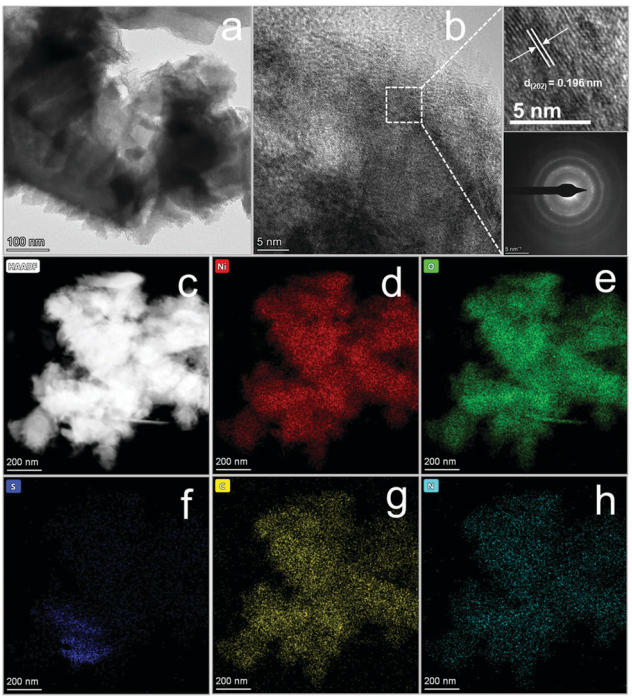

Fig. 6 TEM image (a), HRTEM image (b) and its enlarged lattice fringe image (top) and SAED pattern (down) and elemental mapping images (c–h) of H-Ni_3S_2@NC-3/NF after a long-term *i*–*t* test.

resistance (R_{ct}). The smaller semicircle diameter corresponds to smaller electrochemical impedance of the as-prepared electrode. As shown in Fig. 5e, the lowest R_{ct} of H-Ni_3S_2@NC-3/NF reveals high conductivity of active materials due to the modification of its interlayer carbon.

It is generally acknowledged that a good catalyst shows long-term stability. As depicted in Fig. 5f, H-Ni_3S_2@NC-3/NF exhibits an approximately straight line, indicating the vigorous oxygen evolution process. Furthermore, XRD patterns (Fig. S17a, ESI†) suggest the unchanged crystal structure of Ni_3S_2 except for increased intensity after long-term oxygen production. SEM images (Fig. S17b and d, ESI†) of H-Ni_3S_2@NC-3/NF for post-OER reveal the formation of nanosheet morphology by an electrocatalytic self-oxidation process. The EDS spectrum (Fig. S17c, ESI†) suggests the composition of Ni, S, N, C and O elements, whereas the amount of N elements decreases to an extremely low content. The XPS survey spectrum of H-Ni_3S_2@NC-3/NF for post-OER shows Ni, S, C and O elements (Fig. S18a, ESI†). The N element with an extremely low content is not observed, which is in good agreement with the EDS results (Fig. S17c, ESI†). The slight decrease in current density after 4 h, as shown in Fig. 5f, may be due to the absence of N-doping, confirming the significance of electronic modification. In addition, the high-resolution XPS spectrum of Ni 2p shows high contents of Ni(III), which is ascribed to the surface oxidation during long-term electrocatalytic process.[42] The high-resolution XPS spectrum of S 2p reveals the characteristic peak of S–M, indicating the favorable stability of H-Ni_3S_2@NC-3/NF. Although electrocatalytic self-oxidation leads to N loss, it causes high valence of the Ni center, which is believed to be the effective active site for OERs.[43] Moreover, the TEM image, HRTEM image, SAED pattern, and HAADF-element mapping images of the catalyst after long-term stability are shown in Fig. 6. As shown in Fig. 6a, nanosheets formed on the surface of the catalyst after long-term stability test, which is due to the vigorous electrooxidation of oxygen-containing intermediates. Additionally, the resultant nanosheets show a distinct lattice fringe of 0.196 nm, which is assigned to the (202) plane of Ni_3S_2, as shown in Fig. 6b and its enlarged images. The elemental mapping images (Fig. 6c–h) indicate the composition of Ni, S, C, N, and O elements, which are in full agreement with the above-mentioned results of EDS and XPS. Therefore, this unique H-Ni_3S_2@NC-3/NF with continuous electroactivity is considered as a promising alternative to noble-metal-based catalysts for OERs.

4 Conclusions

In summary, TU-templated synthesis of hierarchical H-Ni_3S_2@NC-3/NF and corresponding growth mechanism are proposed. The self-supporting electrocatalyst has been systematically prepared by a solvothermal method with different reaction factors including temperature, time, content, S source, Ni source and substrate. The growth mechanism demonstrates that nickel–thiourea coordination converts N-doped intercalation into multilayered polyhedron-like Ni_3S_2 with nanosheet-reconstructed broccoli-like Ni_3S_2 grown on the NF substrate spontaneously driven by the addition of nickel that induced diffusion rate differences. Compared with Ni_3S_2/NF, the as-prepared H-Ni_3S_2@NC-3/NF exhibits enhanced OER electrocatalytic performance with an overpotential of 238 mV at a current density of 10 mA cm^{-2} and long-term stability. Our work proposes a new route to fabricate N-doped carbon-intercalated hierarchical metal sulfides as self-supporting electrodes for water splitting.

Conflicts of interest

The authors declare no conflict of interest.

Acknowledgements

This work was financially supported by Sichuan Science and Technology Program (Grant No. 2020YFG0372).

References

1 P. L. McHugh, A. D. Stergiou and M. D. Symes, Decoupled electrochemical water splitting: from fundamentals to applications, *Adv. Energy Mater.*, 2020, **10**, 2002453.
2 X. J. Zhang, A. W. Maijenburg, X. P. Li, S. L. Schweizer and R. B. Wehrspohn, Bifunctional heterostructured transition metal phosphides for efficient electrochemical water splitting, *Adv. Funct. Mater.*, 2020, **30**, 2003261.

3 S. L. Zhang, B. Y. Guan, X. F. Lu, S. B. Xi, Y. H. Du and X. W. Lou, Metal atom-doped Co_3O_4 hierarchical nanoplates for electrocatalytic oxygen evolution, *Adv. Mater.*, 2020, **32**, 2002235.

4 K. Maslana, K. Wenelska, M. Biegun and E. Mijowska, High catalytic performance of tungsten disulphide rodes in oxygen evolution reactions in alkaline solutions, *Appl. Catal., B*, 2020, **266**, 118575.

5 P. P. Li, R. B. Zhao, H. Y. Chen, H. B. Wang, P. P. Wei, H. Huang, Q. Liu, T. S. Li, X. F. Shi, Y. Y. Zhang, M. L. Liu and X. P. Sun, Recent advances in the development of water oxidation electrocatalysts at mild pH, *Small*, 2019, **15**, 1805103.

6 Y. Zhao, J. Bai, X. R. Wu, P. Chen, P. J. Jin, H. C. Yao and Y. Chen, Atomically ultrathin RhCo alloy nanosheet aggregates for efficient water electrolysis in broad pH range, *J. Mater. Chem. A*, 2019, **7**, 16437–16446.

7 N. Yu, W. Cao, M. Huttula, Y. Kayser, P. Hoenicke, B. Beckhoff, F. Y. Lai, R. H. Dong, H. X. Sun and B. Y. Geng, Fabrication of FeNi hydroxides double-shell nanotube arrays with enhanced performance for oxygen evolution reaction, *Appl. Catal., B*, 2020, **261**, 118193.

8 B. Fei, Z. L. Chen, J. X. Liu, H. B. Xu, X. X. Yan, H. L. Qing, M. Chen and R. B. Wu, Ultrathinning nickel sulfide with modulated electron density for efficient water splitting, *Adv. Energy Mater.*, 2020, **10**, 2001963.

9 D. Lim, E. Oh, C. Lim, S. E. Shim and S. H. Baeck, Fe-doped Ni_3S_2 nanoneedles directly grown on Ni foam as highly efficient bifunctional electrocatalysts for alkaline overall water splitting, *Electrochim. Acta*, 2020, **361**, 137080.

10 X. X. Wu, T. Zhang, J. X. Wei, P. F. Feng, X. B. Yan and Y. Tang, Facile synthesis of Co and Ce dual-doped Ni_3S_2 nanosheets on Ni foam for enhanced oxygen evolution reaction, *Nano Res.*, 2020, **13**, 2130–2135.

11 Y. Q. Gong, Z. Yang, Y. Lin, T. Zhou, J. H. Li, F. X. Jiao and W. F. Wang, Controlled synthesis of bifunctional particle-like Mo/Mn-Ni_xS_y/NF electrocatalyst for highly efficient overall water splitting, *Dalton Trans.*, 2019, **48**, 6718–6729.

12 M. Khodabakhshi, S. M. Chen, T. Ye, H. Wu, L. Yang, W. F. Zhang and H. X. Chang, Hierarchical highly wrinkled trimetallic NiFeCu phosphide nanosheets on nanodendrite Ni_3S_2/Ni Foam as an efficient electrocatalyst for the oxygen evolution reaction, *ACS Appl. Mater. Interfaces*, 2020, **12**, 36268–36276.

13 Y. Q. Yang, K. Zhang, H. L. Lin, X. Li, H. C. Chan, L. C. Yang and Q. S. Gao, MoS_2-Ni_3S_2 heteronanorods as efficient and stable bifunctional electrocatalysts for overall water splitting, *ACS Catal.*, 2017, **7**, 2357–2366.

14 Y. Xu, X. J. Chai, T. L. Ren, H. J. Yu, S. L. Yin, Z. Q. Wang, X. N. Li, L. Wang and H. J. Wang, Synergism of interface and electronic effects: bifunctional N-doped Ni_3S_2/N-doped MoS_2 hetero-nanowires for efficient electrocatalytic overall water splitting, *Chem. – Eur. J.*, 2019, **25**, 16074–16080.

15 H. Y. Qin, B. Zhang, Y. P. Pan, X. X. Wang, L. C. Diao, J. Chen, J. L. Wu, E. Z. Liu, J. W. Sha, L. Y. Ma and N. Q. Zhao, Accelerating water dissociation kinetics on Ni_3S_2 nanosheets by P-induced electronic modulation, *J. Catal.*, 2020, **381**, 493–500.

16 W. J. He, L. L. Han, Q. Y. Hao, X. R. Zheng, Y. Li, J. Zhang, C. C. Liu, H. Liu and H. L. L. Xin, Fluorine-anion-modulated electron structure of nickel sulfide nanosheet arrays for alkaline hydrogen evolution, *ACS Energy Lett.*, 2019, **4**, 2905–2912.

17 B. L. Li, Z. S. Li, Q. Pang and J. Z. Zhang, Core/shell cable-like Ni_3S_2 nanowires/N-doped graphene-like carbon layers as composite electrocatalyst for overall electrocatalytic water splitting, *Chem. Eng. J.*, 2020, **401**, 126045.

18 S. M. Dou, J. Xu, X. Y. Cui, W. D. Liu, Z. C. Zhang, Y. D. Deng, W. B. Hu and Y.N. Chen High-temperature, shock enabled nanomanufacturing for energy-related applications, *Adv. Energy Mater.*, 2020, **10**, 2001331.

19 J. B. Li, J. L. Li, Z. B. Ding, X. L. Zhang, Y. Q. Li, T. Lu, Y. F. Yao, W. J. Mai and L. K. Pan, In-situ encapsulation of Ni_3S_2 nanoparticles into N-doped interconnected carbon networks for efficient lithium storage, *Chem. Eng. J.*, 2019, **378**, 122108.

20 S. Wang, W. D. Xue, Y. Fang, Y. Q. Li, L. L. Yan, W. J. Wang and R. Zhao, Bismuth activated succulent-like binary metal sulfide heterostructure as a binder-free electrocatalyst for enhanced oxygen evolution reaction, *J. Colloid Interface Sci.*, 2020, **573**, 150–157.

21 B. X. Wu, H. Qian, Z. W. Nie, Z. P. Luo, Z. X. Wu, P. Liu, H. He, J. H. Wu, S. G. Chen and F. F. Zhang, Ni_3S_2 nanorods growing directly on Ni foam for all-solid-state asymmetric supercapacitor and efficient overall water splitting, *J. Energy Chem.*, 2020, **46**, 178–186.

22 P. Zhou, Y. Q. Wu, C. Wang, H. N. Huang, D. N. Xing, Y. Y. Liu, Z. Y. Wang, P. Wang, Z. K. Zheng, H. F. Cheng, Y. Dai and B. B. Huang, Tailoring the composition and structure of Ni_3S_2 by introduction of Co towards high efficiency energy storage device, *Chem. Eng. J.*, 2021, **403**, 126285.

23 M. R. Guo, A. Qayum, S. Dong, X. L. Jiao, D. R. Chen and T. Wang, In situ conversion of metal (Ni, Co or Fe) foams into metal sulfide (Ni_3S_2, Co_9S_8 or FeS) foams with surface grown N-doped carbon nanotube arrays as efficient super-aerophobic electrocatalysts for overall water splitting, *J. Mater. Chem. A*, 2020, **8**, 9239–9247.

24 F. Guillaume, S. Huang, K. D. M. Harris, M. Couzi and D. Talaga, Optical phonons in millerite (NiS) from single-crystalpolarized Raman spectroscopy, *J. Raman Spectrosc.*, 2008, **39**, 1419–1422.

25 L. L. Feng, G. T. Yu, Y. Y. Wu, G. D. Li, H. Li, Y. H. Sun, T. Asefa, W. Chen and X. X. Zou, High-index faceted Ni_3S_2 nanosheet arrays as highly active and ultrastable electrocatalysts for water splitting, *J. Am. Chem. Soc.*, 2015, **137**, 14023–14026.

26 H. Jiang, J. X. Gu, X. S. Zheng, M. Liu, X. Q. Qiu, L. B. Wang, W. Z. Li, Z. F. Chen, X. B. Ji and J. Li, Defect-rich and ultrathin N doped carbon nanosheets as advanced trifunctional metal-free electrocatalysts for the ORR, OER and HER, *Energy Environ. Sci.*, 2019, **12**, 322–333.

27 H. X. Jia, Y. C. Yao, J. T. Zhao, Y. Y. Gao, Z. L. Luo and P. W. Du, A novel two-dimensional nickel phthalocyanine-based metal-organic framework for highly efficient water oxidation catalysis, *J. Mater. Chem. A*, 2018, **6**, 1188–1195.

28 G. F. Chen, T. Y. Ma, Z. Q. Liu, N. Li, Y. Z. Su, K. Davey and S. Z. Qiao, Efficient and stable bifunctional electrocatalysts Ni/Ni_xM_y (M = P, S) for overall water splitting, *Adv. Funct. Mater.*, 2016, **26**, 3314–3323.

29 Y. Yang, H. Q. Yao, Z. H. Yu, S. M. Islam, H. Y. He, M. W. Yuan, Y. H. Yue, K. Xu, W. C. Hao, G. B. Sun, H. F. Li, S. L. Ma, P. Zapol and M. G. Kanatzidis, Hierarchical nanoassembly of $MoS_2/Co_9S_8/Ni_3S_2/Ni$ as a highly efficient electrocatalyst for overall water splitting in a wide pH range, *J. Am. Chem. Soc.*, 2019, **141**, 10417–10430.

30 H. C. Yang, C. H. Wang, Y. J. Zhang and Q. B. Wang, Chemical valence-dependent electrocatalytic activity for oxygen evolution reaction: a case of nickel sulfides hybridized with N and S Co-doped carbon nanoparticles, *Small*, 2018, **14**, 1703273.

31 H. Wu, Q. Lu, J. F. Zhang, J. J. Wang, X. P. Han, N. Q. Zhao, W. B. Hu, J. J. Li, Y. N. Chen and Y. D. Deng, Thermal shock-activated spontaneous growing of nanosheets for overall water splitting, *Nano-Micro Lett.*, 2020, **12**, 162.

32 Z. Cui, Y. C. Ge, H. Chu, R. Baines, P. Dong, J. H. Tang, Y. Yang, P. M. Ajayan, M. X. Ye and J. F. Shen, Controlled synthesis of Mo-doped Ni_3S_2 nano-rods: an efficient and stable electro-catalyst for water splitting, *J. Mater. Chem. A*, 2017, **5**, 1595–1602.

33 Y. N. Chen, S. M. Xu, S. Z. Zhu, R. J. Jacob, G. Pastel, Y. B. Wang, Y. J. Li, J. Q. Dai, F. J. Chen, H. Xie, B. Y. Liu, Y. G. Yao, L. G. Salamanca-Riba, M. R. Zachariah, T. Li and L. B. Hu, Millisecond synthesis of CoS nanoparticles for highly efficient overall water splitting, *Nano Res.*, 2019, **12**, 2259–2267.

34 L. X. Wang, Y. Li, X. C. Yin, Y. Z. Wang, A. L. Song, Z. P. Ma, X. J. Qin and G. J. Shao, Coral-like structured Ni/C_3N_4 composite coating: an active electrocatalyst for hydrogen evolution reaction in alkaline solution, *ACS Sustainable Chem. Eng.*, 2017, **5**, 7993–8003.

35 D. Tian, N. Song, M. X. Zhong, X. F. Lu and C. Wang, Bimetallic MOF nanosheets decorated on electrospun nanofibers for high-performance asymmetric supercapacitors, *ACS Appl. Mater. Interfaces*, 2020, **12**, 1280–1291.

36 Y. Hou, M. Qiu, M. G. Kim, P. Liu, G. Nam, T. Zhang, X. D. Zhuang, B. Yang, J. Cho, M. W. Chen, C. Yuan, L. C. Lei and X. L. Feng, Atomically dispersed nickel-nitrogen-sulfur species anchored on porous carbon nanosheets for efficient water oxidation, *Nat. Commun.*, 2019, **10**, 1392.

37 H. Z. Xu, K. Zhu, J. L. Yin, J. Yan, G. L. Wang and D. X. Cao, Efficient bifunctional catalysts synthesized from three-dimensional Ni/Fe bimetallic organic frameworks for overall urea electrolysis, *Dalton Trans.*, 2020, **49**, 5646–5652.

38 B. H. An, J. C. Li, X. C. Wu, W. Q. Li, Y. L. Li, L. N. Sun, H. W. Mi, Q. L. Zhang, C. X. He and X. Z. Ren, One-pot synthesis of N,S-doped pearl chain tube-loaded Ni_3S_2 composite materials for high-performance lithium-air batteries, *Nanoscale*, 2020, **12**, 21770–21779.

39 C. Liu, W. Zhou, J. F. Zhang, Z. L. Chen, S. L. Liu, Y. Zhang, J. X. Yang, L. Y. Xu, W. B. Hu, Y. N. Chen and Y.D. Deng Air-assisted, transient synthesis of metastable nickel oxide boosting alkaline fuel oxidation reaction, *Adv. Energy Mater.*, 2020, **10**, 2001397.

40 W. J. Zhou, X. J. Wu, X. H. Cao, X. Huang, C. L. Tan, J. Tian, H. Liu, J. Y. Wang and H. Zhang, Ni_3S_2 nanorods/Ni foam composite electrode with low overpotential for electrocatalytic oxygen evolution, *Energy Environ. Sci.*, 2013, **6**, 2921–2924.

41 X. Zou, Y. P. Liu, G. D. Li, Y. Y. Wu, D. P. Liu, W. Li, H. W. Li, D. J. Wang, Y. Zhang and X. X. Zou, Ultrafast formation of amorphous bimetallic hydroxide films on 3D conductive sulfide nanoarrays for large-current-density oxygen evolution electrocatalysis, *Adv. Mater.*, 2017, **29**, 1700404.

42 J. Jiang, S. Lu, H. Gao, X. Zhang and H. Q. Yu, Ternary $FeNiS_2$ ultrathin nanosheets as an electrocatalyst for both oxygen evolution and reduction reactions, *Nano Energy*, 2016, **27**, 526–534.

43 B. H. Cui, Z. Hu, C. Liu, S. L. Liu, F. S. Chen, S. Hu, J. F. Zhang, W. Zhou, Y. D. Deng, Z. B. Qin, Z. Wu, Y. A. Chen, L. F. Cui and W. B. Hu, Heterogeneous lamellar-edged Fe-$Ni(OH)_2/Ni_3S_2$ nanoarray for efficient and stable seawater oxidation, *Nano Res.*, 2021, **14**, 1149–1155.